

Numerical Implementation of Non-Markovian Quantum State Diffusion

Joshua Wilkie and Ray Ng

*Department of Chemistry, Simon Fraser University,
Burnaby, British Columbia V5A 1S6, Canada*

(Dated: July 24, 2018)

Abstract

Non-Markovian quantum state diffusion (NMQSD) is a non-relativistic but otherwise exact theory which expresses the reduced density matrix of an arbitrary subsystem, interacting linearly with an uncoupled harmonic oscillator bath, as an average of diadics formed from state vectors which obey stochastic variational-differential equations. The vacuum radiation field can be represented as such an oscillator bath, and so this model is in widespread use in quantum optics. Prior to the development of NMQSD, exact subsystem solutions could only be obtained in a few special cases (e.g. spin-1/2, harmonic oscillator). Unfortunately, it has not yet been possible to obtain exact solutions to new problems using NMQSD due to the difficulty of solving the variational-differential equations. Here we show that these equations can be transformed into a pair of coupled nonlinear integrodifferential equations. We develop exact numerical methods for the integrodifferential equations and show that solutions can be readily obtained to good accuracy for quite general subsystems. We exactly solve various examples including tunneling in a double well representing molecular isomerization or racemization, suppression of fluorescence from a two-level atom in a band gap, and intermittent fluorescence from a driven three level system representing electronic states of singly ionized magnesium.

I. INTRODUCTION

Few-level or few-body quantum systems such as single (or few chemically reacting) trapped atomic[1] or molecular ions in ion traps, interacting with lasers and the vacuum, are systems of considerable current interest. Intermittent single ion fluorescence has been studied experimentally[1] and theoretically[2, 3, 4, 5]. Ions in traps have also served as models of quantum computers[6]. These systems can all be accurately modeled as a subsystem interacting linearly with a bath of harmonic oscillators. Exact solutions for this model have only been obtained for restrictive cases where the subsystem consists of a spin-1/2[7, 8] or a harmonic oscillator[9, 10], and in a few other special cases. Theoretical studies of such systems have therefore usually relied on approximate master equations[2, 3], jump theories[4] and Markovian stochastic Schrödinger equations[5]. Nevertheless, a theory yielding exact solutions for this model for general subsystem Hamiltonians would have widespread applications. Such a theory could also prove useful as a limiting case for development of theories for subsystem evolution under the influence of more general baths (e.g. single quantum-dot [12] and single-molecule[13] fluorescence in condensed phase environments) for which theory is still in the early stages of development[13, 14], and for which intra-bath coupling is expected to play an important role[15].

In a formal sense the problem of an arbitrary subsystem interacting linearly with an uncoupled oscillator bath has recently been solved. The first important contribution toward this theory[11] showed that the influence functional has a particularly simple form. Subsequently it was shown that the exact reduced subsystem density, expressed as a path integral weighted by the influence functional, can be stochastically unraveled as an average over diadics constructed from state vectors which obey a non-Markovian variational-differential wave equation[17, 18, 19]. The resulting exact theory has been called non-Markovian quantum state diffusion (NMQSD), and from NMQSD one can *in principle* obtain exact solutions of the subsystem-oscillator bath model for any subsystem.

In practice, no new exact solutions have been obtained using NMQSD. While exact evolution equations can be formulated for any subsystem, these equations contain variational derivatives with respect to the complex colored noises which emerge during the stochastic unraveling. Variational-differential equations (VDEs) have not received the same attention as partial differential equations and much less is known about their properties and solutions.

As a consequence the evolution equation has proved impossible to solve - even numerically - except for the few models for which exact solutions were previously known[17, 18, 19]. This impasse has led to the introduction of various perturbative expansions[20, 21] and numerical approximation schemes[22]. However, direct and exact methods for solution of the NMQSD equations remain an important goal.

Direct solution of the NMQSD equations may eventually be possible, but for the present methods which circumvent the problem by eliminating the variational derivative seem most promising. This manuscript introduces a pair of coupled nonlinear stochastic integrodifferential equations which we show are exactly equivalent to the stochastic VDE of NMQSD. Integrodifferential evolution equations can be converted to ordinary or partial differential equations[23, 24]. Hence, the pair of stochastic integrodifferential equations can be converted to stochastic ordinary or partial differential equations which are easier to solve. Recently developed numerical methods allow efficient solution of stochastic (ordinary and partial) differential equations (SDEs)[25, 26] even for quite large systems of equations[27]. On the basis of the transformed equations and using these SDE integrators we develop exact numerical methods for solving NMQSD problems. Example calculations for which exact solutions are known are used to verify the accuracy and efficiency of the new methods. We also numerically solve three new problems which were previously intractable.

Equivalent linear and nonlinear formulations of NMQSD exist. The nonlinear version of the theory preserves the norm of the state vector, which results in improved Monte Carlo convergence. Accordingly, we also consider linear and nonlinear reformulations of NMQSD. The simpler linear version is considered in section II, while the nonlinear case is treated in section III. Simple example calculations are used to illustrate the two approaches. More interesting applications to a tunneling problem representing molecular isomerization or recemization, to suppression of fluorescence from a two-level atom in a dielectric band gap, and to a driven three level system exhibiting intermittent fluorescence, are considered in section IV.

II. LINEAR NMQSD EQUATIONS

Consider for simplicity a subsystem-bath model with a single subsystem coupling operator L . The total Hamiltonian is

$$H_{tot} = H + \sum_{\omega} g_{\omega}(La_{\omega}^{\dagger} + L^{\dagger}a_{\omega}) + \sum_{\omega} \omega a_{\omega}^{\dagger}a_{\omega} \quad (1)$$

where we are using units in which $\hbar = 1$. Here H is the subsystem Hamiltonian, g_{ω} is a coupling constant for an oscillator mode of frequency ω , and the rest of the notation should be clear. The generalization of NMQSD and our results to multiple subsystem coupling operators is straightforward, so we will confine our attention to this simplest case.

In NMQSD the evolution of the state vector ψ_t is governed by the linear VDE

$$\frac{d\psi_t}{dt} = -iH \psi_t + z_t L \psi_t - L^{\dagger} \int_0^t ds \alpha(t, s) \frac{\delta\psi_t}{\delta z_s} \quad (2)$$

where z_t is a complex colored noise with correlation function

$$\alpha(t, s) = M[z_t^* z_s]. \quad (3)$$

In the limit of zero temperature $\alpha(t, s) = \sum_{\omega} g_{\omega}^2 e^{-i\omega(t-s)}$ (see Refs. [17, 18, 19] for the non-zero temperature formula). Here $M[...]$ denotes the average over different realizations of the noise. The exact reduced density matrix ρ_t of the subsystem is given as an average of diadics via $\rho_t = M[|\psi_t\rangle\langle\psi_t|]$.

The solution ψ_t of (2) is known to be an analytic functional of the noise z_t [18] and so the variational derivative is well defined. The presence of this variational derivative does however make the evolution equation difficult to solve. In some simple cases one can guess the form of $\frac{\delta\psi_t}{\delta z_s}$ and use a self-consistency requirement to find solutions of Eq. (2). Other than these few examples, it is generally unclear whether it is possible to directly solve the VDE (2) since numerical algorithms for VDEs have not yet been developed. Fortunately, it is possible to reformulate the theory in terms of more easily solved integrodifferential equations.

To start with our reformulation, we introduce a non-unitary propagator $U(t, s)$ which evolves a state vector from time s to time t . If we consider subsystem evolution from a state ψ_0 at time 0 then $\psi_t = U(t, 0)\psi_0$. From Eq. (2) we deduce that

$$\frac{dU(t, 0)}{dt} = -iH U(t, 0) + z_t L U(t, 0) - L^{\dagger} \int_0^t ds \alpha(t, s) \frac{\delta U(t, 0)}{\delta z_s}. \quad (4)$$

Next we need to eliminate the variational derivative $\frac{\delta U(t,0)}{\delta z_s}$. In particular, we will show that

$$\frac{\delta U(t,0)}{\delta z_s} = U(t,s) L U(s,0). \quad (5)$$

Consider for simplicity the case where L has a complete eigenbasis $|x\rangle$ which can be used to construct a path integral for the propagator along the lines followed in Ref. [17]. The path integral representation of $U(t,0)$ is a sum over paths weighted by an exponential whose argument includes a stochastic term $\int_0^t du z_u x_u$, where $L|x_u\rangle = x_u|x_u\rangle$ and $|x_u\rangle$ for each value of u denotes an element of some complete basis (i.e. the path integral is over all x_u for each value of u between 0 and t) [17, 18, 19]. The variational derivative of $U(t,0)$ with respect to z_s thus brings down a prefactor $\int_0^t du \frac{\delta z_u}{\delta z_s} x_u$ inside the path integral. Using the fact that

$$\frac{\delta z_u}{\delta z_s} = \delta(u-s) \quad (6)$$

and removing the closure relation for x_s at time s we then obtain Eq. (5).

Now Eq. (5) and the semigroup property

$$U(t,s) = U(t,0)U(s,0)^{-1} \quad (7)$$

allow us to rewrite Eq. (4) in the form

$$\frac{dU(t,0)}{dt} = -iH U(t,0) + z_t L U(t,0) - L^\dagger U(t,0) \int_0^t ds \alpha(t,s) U(s,0)^{-1} L U(s,0), \quad (8)$$

which is a nonlinear integrodifferential equation for $U(t,0)$. This equation is exact and entirely equivalent to Eq. (2). No loss of generality is incurred in working with Eq. (8), but in a finite basis set the number of equations arising from (8) is the square of the number of equations arising from Eq. (2). Moreover, Eq. (8) is clearly nonlinear whereas Eq. (2) is linear in at least some cases. These apparent defects are unfortunate, but one must recognize that Eq. (8) is solvable while (2) is not, and the computational costs of solving (8) are quite reasonable for a large class of potentially interesting problems. We solve three such examples in section IV. Thus, implementations and applications of (8) and its norm-preserving generalizations are the focus of this manuscript.

Direct inversion of $U(s,0)$, required for (8), can be avoided at the expense of adding a second equation. Consider the dynamics of $U(0,t) = U(t,0)^{-1}$. Using the fact that

$U(0, t)U(t, 0) = 1$ and differentiating with respect to t gives

$$\begin{aligned} \frac{dU(0, t)}{dt}U(t, 0) + U(0, t)\{-iHU(t, 0) + z_tLU(t, 0) \\ -L^\dagger U(t, 0) \int_0^t ds \alpha(t, s)U(s, 0)^{-1}LU(s, 0)\} = 0. \end{aligned} \quad (9)$$

Multiplying on the left by $U(t, 0)^{-1}$ then gives

$$\frac{dU(0, t)}{dt} + U(0, t)\{-iH + z_tL - L^\dagger U(t, 0) \int_0^t ds \alpha(t, s)U(s, 0)^{-1}LU(s, 0)U(0, t)\} = 0 \quad (10)$$

or

$$\begin{aligned} \frac{dU(0, t)}{dt} &= iU(0, t)H - z_tU(0, t)L \\ &+ U(0, t)L^\dagger U(t, 0) \int_0^t ds \alpha(t, s)U(s, 0)^{-1}LU(s, 0)U(0, t) \end{aligned} \quad (11)$$

which is again of integrodifferential form. Note that both equations (8) and (11) involve only $U(t, 0)$ and $U(t, 0)^{-1}$ so that the pair is closed.

Changing notation to $U_t = U(t, 0)$ and $U_t^{-1} = U(0, t)$ we can rewrite equations (8) and (11) as

$$\begin{aligned} \frac{dU_t}{dt} &= -iH U_t + z_tL U_t - L^\dagger U_t \int_0^t ds \alpha(t, s)U_s^{-1}L U_s \\ \frac{dU_t^{-1}}{dt} &= iU_t^{-1} H - z_tU_t^{-1}L + U_t^{-1}L^\dagger U_t \int_0^t ds \alpha(t, s)U_s^{-1}L U_s U_t^{-1} \end{aligned} \quad (12)$$

which is a closed set of integrodifferential equations. We will now show that Eqs. (12) can be transformed into sets of ordinary or partial differential equations.

The most efficient set of transformed equations depends on the properties of the memory function. In section IIA we assume that the memory function consists of a few terms of exponential form, i.e.,

$$\alpha(t, s) = \sum_{j=1}^m A_j e^{-\gamma_j|t-s|} e^{-i\omega_j(t-s)} \quad (13)$$

where A_j and γ_j are positive numbers. The terms in Eq. (13) do not in general correspond to physical bath oscillator modes. Instead Eq. (13) can be viewed as a best fit to the memory function, obtained by nonlinear least squares[23] or other techniques[28]. In many cases the number of required terms m can be quite small. The general case where m is very large, or where $\alpha(t, s)$ cannot be written in the form (13), is considered in section IIB. To illustrate the application of these methods we numerically solve a number of example problems. For

each example problem, Eqs. (12) are expressed in ordinary differential form and solved using stochastic integration methods[25, 26].

Colored noises can be generated using a variety of techniques[21, 29, 30]. We chose memory functions for our examples which can be expressed via Eq. (13). The complex colored noise is then generated via $z_t = \sum_{j=1}^m \xi_t^j$ by integrating the stochastic differential equations

$$d\xi_t^j = -(\gamma_j + i\omega_j)\xi_t^j dt + \sqrt{2\gamma_j A_j} dW_t^j \quad (14)$$

from $-\infty$ (in practice some large negative time) to time $t = 0$, and then from $t = 0$ onward in combination with transformed versions of Eqs. (12). Here W_t^j are complex Wiener processes satisfying $M[dW_t^{j*} dW_s^k] = \sqrt{dt} \delta_{j,k} \delta_{t,s}$ and $M[dW_t^j dW_s^k] = 0$. One can show that

$$\xi_t^j = \sqrt{2\gamma_j A_j} \int_{-\infty}^t dW_s^j e^{-\gamma_j(t-s)} e^{-i\omega_j(t-s)}, \quad (15)$$

$z_t = \sum_{j=1}^m \xi_t^j$, and Eq. (3) yield the correct memory function (13) in the mean. The stochastic differential equations (14) are obtained by differentiating expressions (15) for ξ_t^j . Sets of stochastic differential equations like (14) and the transformed versions of (12) can be solved to any required tolerance using recently developed high order variable stepsize integration methods[25, 26].

A. Sum of exponentials

In many cases it is possible to expand the memory function as a sum of a few exponentials of the form Eq. (13). Fits to expansions of this type can be obtained using nonlinear least squares algorithms. In practice, obtaining good fits with nonlinear least squares can be a frustratingly time consuming endeavor. The nonlinearity of the fitting function makes minimization algorithms highly sensitive to the parameter search domains. In such cases, it may be possible to obtain expansions of the same form using other techniques[28].

Once this expansion is known we can define operators

$$V_{t,j} = \int_0^t ds A_j e^{-\gamma_j(t-s)} e^{-i\omega_j(t-s)} U_s^{-1} L U_s \quad (16)$$

such that the full set of equations in ordinary differential form becomes

$$\frac{dU_t}{dt} = -i H U_t + z_t L U_t - L^\dagger U_t \sum_{j=1}^m V_{t,j}$$

$$\begin{aligned}
\frac{dU_t^{-1}}{dt} &= iU_t^{-1}H - z_t U_t^{-1}L + U_t^{-1}L^\dagger U_t \sum_{j=1}^m V_{t,j} U_t^{-1} \\
\frac{dV_{t,j}}{dt} &= -(\gamma_j + i\omega_j)V_{t,j} + A_j U_t^{-1} L U_t.
\end{aligned} \tag{17}$$

Efficient implementation of these equations requires that $\sum_{j=1}^m V_{t,j}$ be computed first and stored temporarily. From this quantity $U_t \sum_{j=1}^m V_{t,j}$ and $L^\dagger U_t \sum_{j=1}^m V_{t,j}$ can be calculated. Numerically it is easier to use the fact that $U_t U_t^{-1} = 1$ and hence that $dU_t^{-1}/dt = -U_t^{-1} dU_t/dt U_t^{-1}$ to find dU_t^{-1}/dt than to program the above equation.

To illustrate the utility of the method we will apply the transformed equations to a few problems where exact solutions are known. In all cases the SDEs were solved using the ANISE software[26]. We also used a single processor for each calculation, but of course one of the primary numerical advantages of quantum state diffusion theories is that they are inherently parallel and should ideally be implemented on clusters. With the exception of example IIC the calculations took only a few minutes.

1. Example IIA

Consider the special case where $H = (\omega/2)\sigma_z$ and $L = \lambda\sigma_z$ and pick $\alpha(t,s) = (\gamma/2)e^{-\gamma(t-s)}$ with $\omega = 1$, $\lambda^2 = 2\omega$ and $\gamma = \omega$. We chose the initial condition $|\psi_0\rangle = \frac{1+2i}{\sqrt{7}}|1\rangle + \frac{1+i}{\sqrt{7}}|2\rangle$ where $\sigma_z|i\rangle = (-1)^{i-1}|i\rangle$ for $i = 1, 2$ (this is the same convention as in Ref. [18]). We calculated $\langle 1|\rho_t|2\rangle$ using Eqs. (17) and an average over 10000 trajectories. In Fig. 1 we plot the real (solid curve) and imaginary (dotted curve) parts vs time against the corresponding known exact results[18] (dashed and dot-dashed, respectively). The accuracy is already very good. In Fig. 2 we plot the diagonal elements of ρ_t which are supposed to be constant for this model. We see that the numerically calculated $\langle 1|\rho_t|1\rangle$ (solid curve) while initially equal to $5/7$ (dashed line) decays away from this value as time proceeds. Similar results are observed for the element $\langle 2|\rho_t|2\rangle$ (dotted curve) which starts at $2/7$ (dot-dashed line) and grows. Hence, for 10000 trajectories convergence is still incomplete for the diagonal elements. We will show in section III that introducing norm-preserving equations will lead to faster convergence.

We also show in Fig. 3 the memory function calculated numerically using the stochastic process z_t (solid curve) and the exact memory function $.5e^{-t}$ (dashed curve). Agreement is satisfactory.

FIG. 1: $\langle 1|\rho_t|2\rangle$ for Example IIA

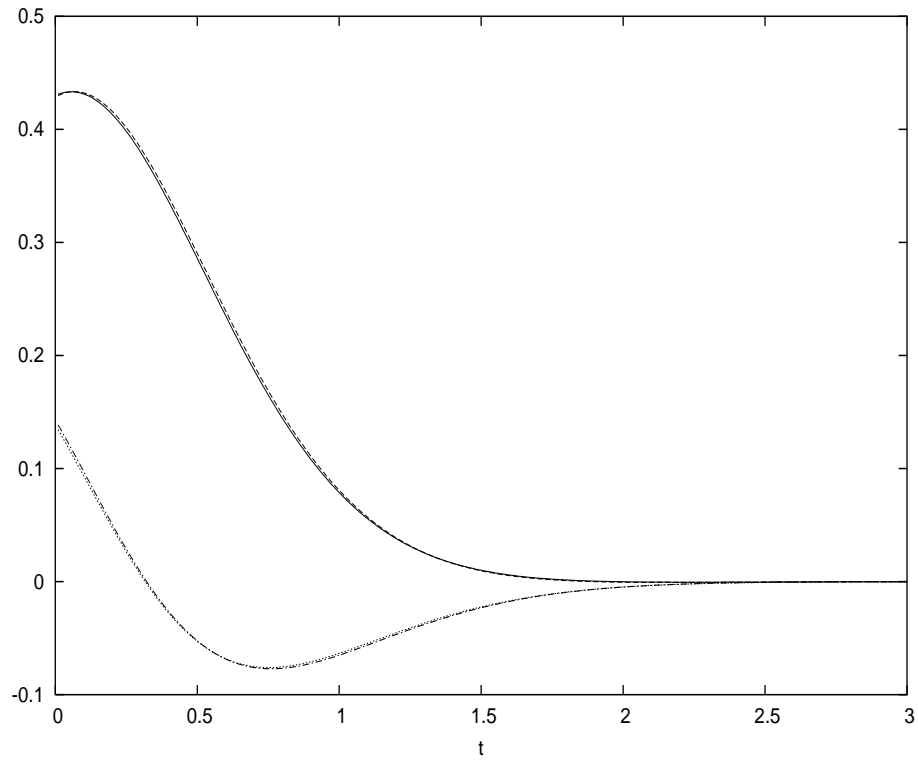


FIG. 2: $\langle 1|\rho_t|1\rangle$ and $\langle 2|\rho_t|2\rangle$ for Example IIA

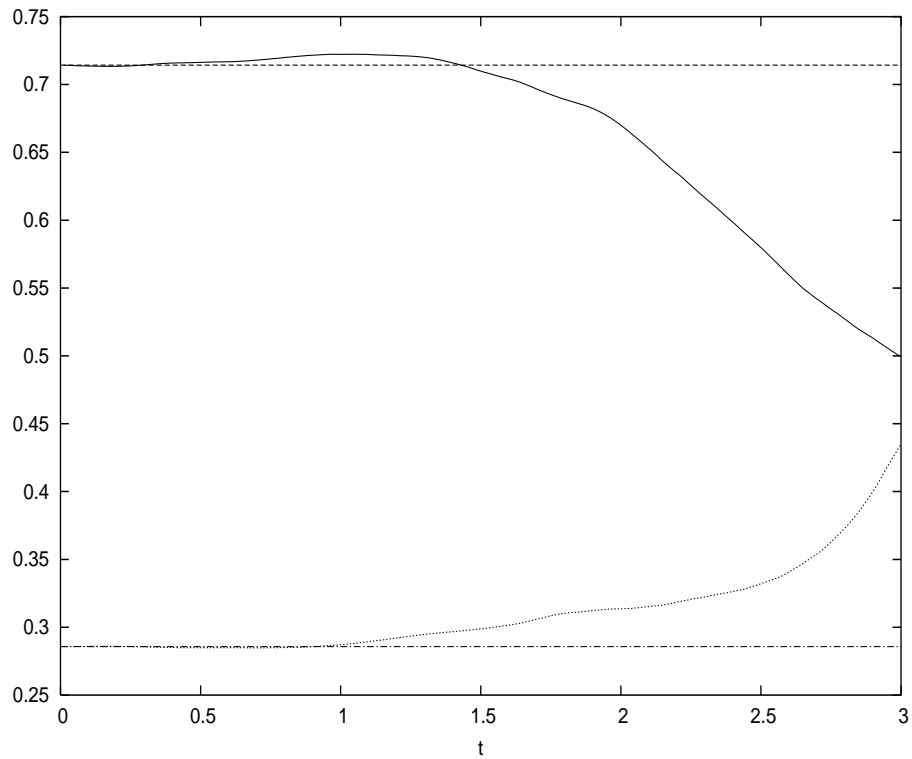
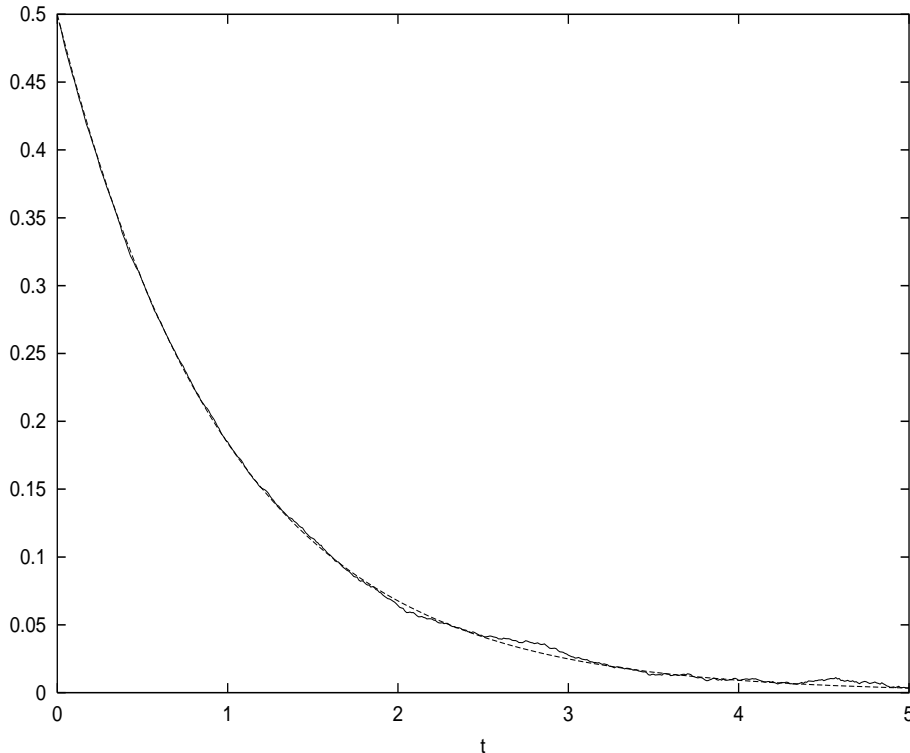


FIG. 3: $\alpha(t,0)$ for Example IIA



2. Example IIB

Now consider the case where $H = (\omega/2)\sigma_z$ and $L = (\lambda/2)(\sigma_x - i\sigma_y)$ (Example IIIB in Ref. [18]) and again pick $\alpha(t,s) = (\gamma/2)e^{-\gamma(t-s)}$ with $\omega = 1$, $\lambda^2 = 2\omega$ and $\gamma = \omega$. For the initial condition $|\psi_0\rangle = \frac{1}{\sqrt{2}}(|1\rangle + |2\rangle)$ we again calculated $\langle 1|\rho_t|2\rangle$ using Eqs. (17) and an average over 10000 trajectories. In Fig. 4 we plot the real (solid curve) and imaginary (dotted curve) parts vs time against the corresponding known exact results[18] (dashed and dot-dashed, respectively). Good agreement is obtained. Figure 5 shows the diagonal matrix elements $\langle 1|\rho_t|1\rangle$ and $\langle 2|\rho_t|2\rangle$ plotted against their corresponding exact results. The results here are also good.

3. Example IIC

Finally, consider a harmonic oscillator subsystem with $H = \omega a^\dagger a$ and $L = \lambda a$. We chose an initial condition $|\psi_0\rangle = \frac{1+2i}{\sqrt{7}}|0\rangle + \frac{1+i}{\sqrt{7}}|1\rangle$ (where $a^\dagger a|n\rangle = n|n\rangle$ for $n = 0, 1, \dots$) and picked $\alpha(t,s) = (\gamma/2)e^{-\gamma(t-s)}$ with $\omega = 1$, $\lambda = \omega$ and $\gamma = \omega$. A basis set consisting of the first five

FIG. 4: $\langle 1|\rho_t|2\rangle$ for Example IIB

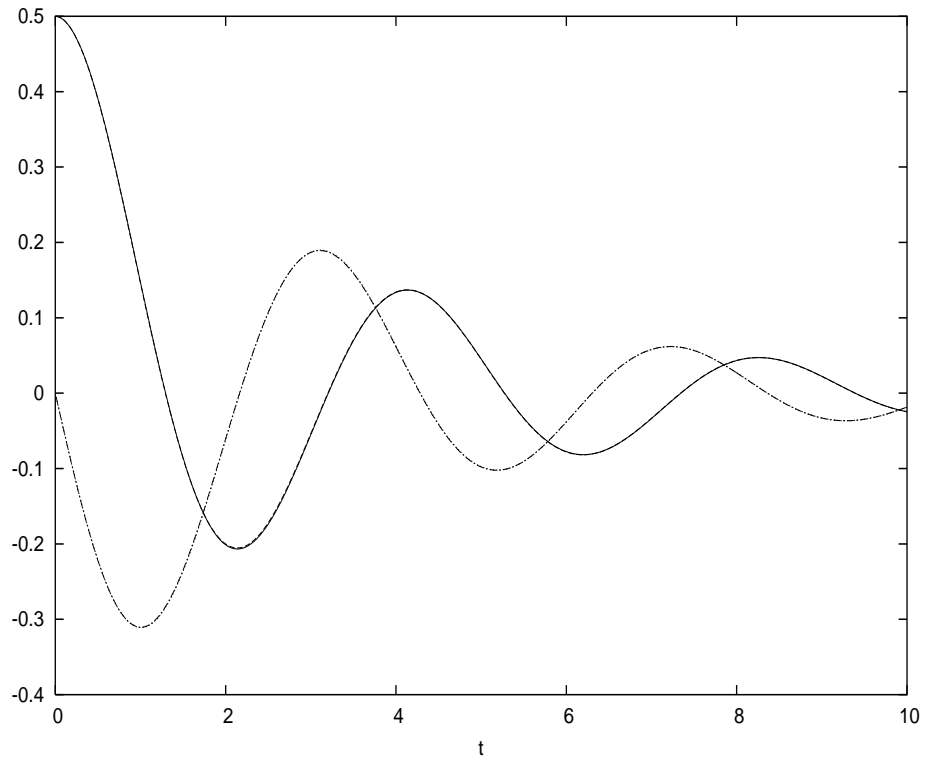
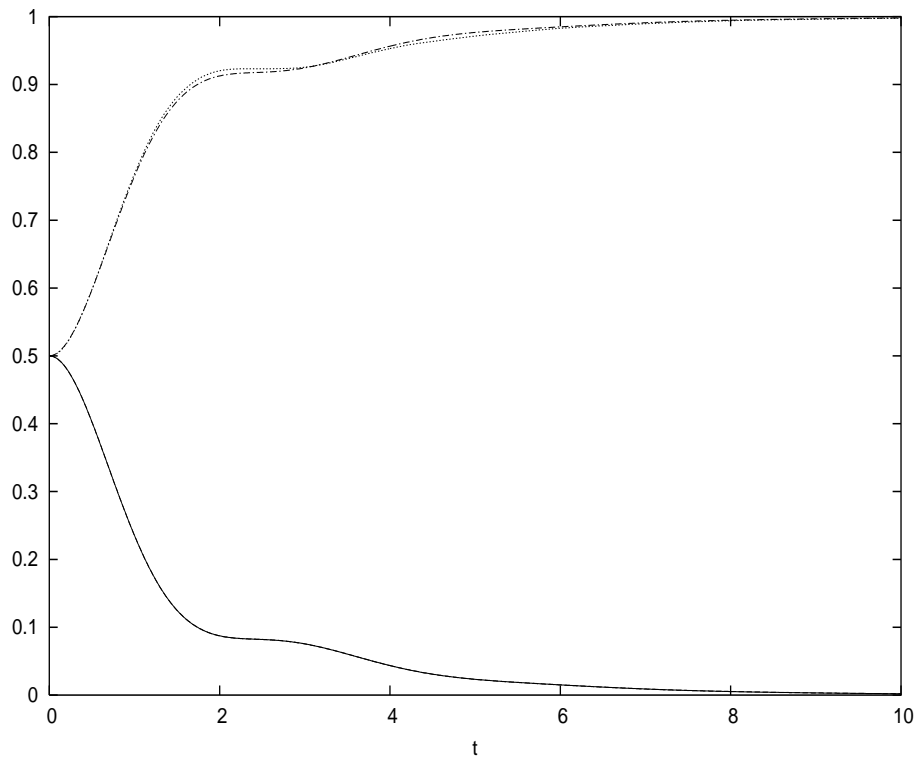
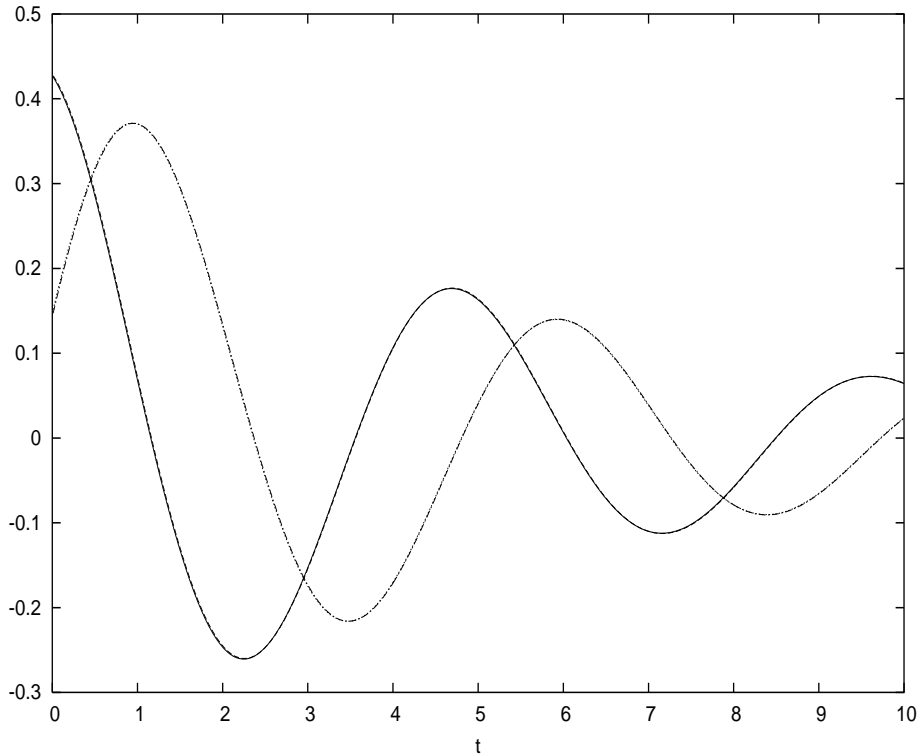


FIG. 5: $\langle 1|\rho_t|1\rangle$ and $\langle 2|\rho_t|2\rangle$ for Example IIB



oscillator states was employed. We computed 10000 trajectories to construct the average. The cpu time was about 114 minutes on a 600 MHz Alpha processor. In Fig. 6 we plot the real and imaginary parts of $\langle 1|\rho_t|2\rangle$ (solid and dotted) vs their corresponding exact real and imaginary parts (dashed and dot-dashed). In Fig. 7 we show that diagonal matrix elements $\langle 1|\rho_t|1\rangle$ and $\langle 2|\rho_t|2\rangle$ (solid and dotted) plotted against their corresponding exact results (dashed and dot-dashed). The results are uniformly good.

FIG. 6: $\langle 1|\rho_t|2\rangle$ for Example IIC

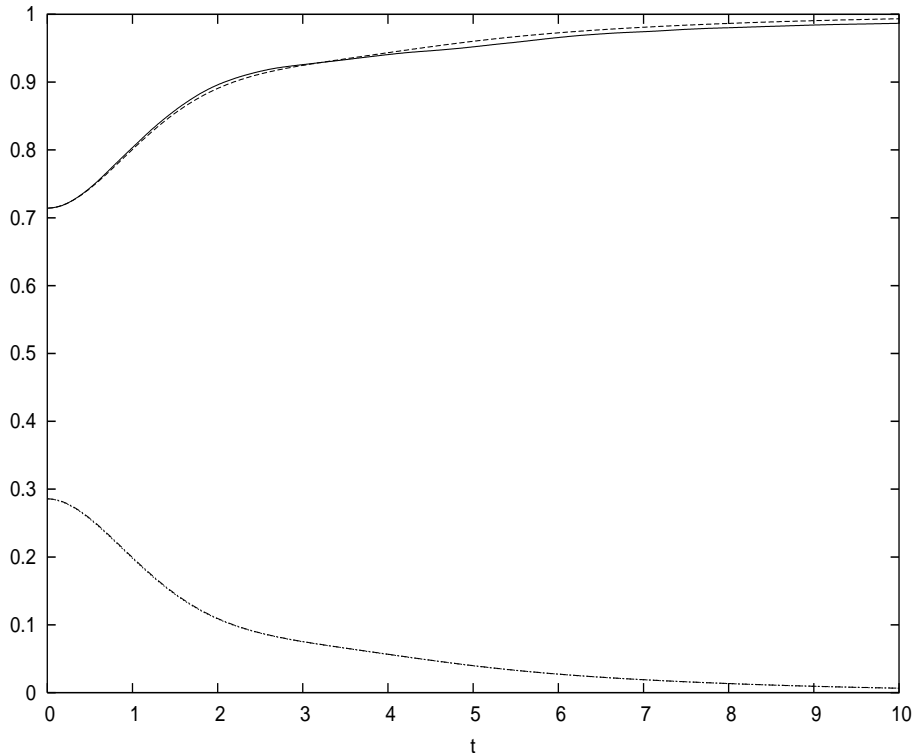


B. General memory function

Here we consider the opposite case where the memory function cannot be efficiently represented as a sum of exponential terms like (13). In this case it may still be desirable to generate the colored noise using Eqs. (14), but otherwise the noise can be generated with spectral methods and other techniques[21, 29, 30]. The key point is that Eqs. (17) will not be efficient and some new approach must be explored.

Equations (12) are of integrodifferential form. Such equations can be solved exactly using a recently developed method[24]. The trick is to convert the equations to partial differential

FIG. 7: $\langle 1|\rho_t|1\rangle$ and $\langle 2|\rho_t|2\rangle$ for Example IIC



form. To do this we introduce a new variable u (where $u \in (-\infty, \infty)$) and define

$$V_{t,u} = \int_0^t ds \alpha(t+u,s)U_s^{-1}LU_s. \quad (18)$$

Differentiating we find that the new set of equations has a partial differential form

$$\begin{aligned} \frac{dU_t}{dt} &= -iHU_t + z_tLU_t - L^\dagger U_t V_{t,0} \\ \frac{dU_t^{-1}}{dt} &= iU_t^{-1}H - z_tU_t^{-1}L + U_t^{-1}L^\dagger U_t V_{t,0}U_t^{-1} \\ \frac{dV_{t,u}}{dt} &= \alpha(t+u,t)U_t^{-1}LU_t + \frac{\partial V_{t,u}}{\partial u} \end{aligned} \quad (19)$$

which is exactly equivalent to the original integrodifferential set (12). The partial derivative $\frac{\partial V_{t,u}}{\partial u}$ can be evaluated using fast Fourier transform methods or using discrete variable representations[24, 31], or by employing a harmonic oscillator basis. In the first two cases the variable u is represented on a grid of points, while a discrete basis is used in the third, and so Eqs. (19) revert to ordinary differential form and hence they can also be solved using the method of Ref. [25] or using the ANISE software[26].

In practice there are advantages to modifying the above equations somewhat by instead

defining

$$V_{t,u} = f(u) \int_0^t ds \alpha(t+u, s) U_s^{-1} L U_s \quad (20)$$

where $f(u) = 1$ and where $f(u)$ decays rapidly with u . These can lead to a smaller required basis set[24] and hence faster algorithms. The modified $V_{t,u}$ obeys

$$\frac{dV_{t,u}}{dt} = f(u) \alpha(t+u, t) U_t^{-1} L U_t + \frac{\partial V_{t,u}}{\partial u} - \frac{f'(u)}{f(u)} V_{t,u} \quad (21)$$

while the equations for U_t and U_t^{-1} are unaltered. We will not explore the issue of which is the optimal form for $f(u)$, but merely note that some success has been had with $f(u) = e^{-\alpha u^2}$ [24]. In the case where the u degree of freedom is represented in an oscillator basis, $f(u)$ should be chosen so that the oscillator matrix elements $\langle n | f(u) \alpha(t+u, t) | m \rangle$ are nonzero only for the first few basis functions.

Finally, we note that it is possible to use a similar trick to generate the complex noise z_t when it is stationary, i.e. when $\alpha(t, s) = c(t-s)$ [21, 29]. Define

$$z_t = \int_{-\infty}^t dW_s R(t-s) \quad (22)$$

with $R(t) = 0$ for $t < 0$, and where dW_s is a differential Wiener process with properties $M[dW_t^* dW_s] = \sqrt{dt} \delta_{t,s}$ and $M[dW_t dW_s] = 0$. It follows that

$$M[z_t^* z_s] = \int_{-\infty}^{\infty} d\tau R^*(\tau) R(\tau - t) \quad (23)$$

from which one can show that

$$R(t) = \frac{1}{\sqrt{2\pi}} \int_{-\infty}^{\infty} d\omega G(\omega) e^{i\omega t} \quad (24)$$

$$|G(\omega)|^2 = \frac{1}{2\pi} \int_{-\infty}^{\infty} dt c(t) e^{i\omega t}. \quad (25)$$

One can then choose $G(\omega) = \sqrt{|G(\omega)|^2}$ (see Refs. [21, 29]).

Now that we have the representation (22) for the noise we can define

$$z_{t,u} = f(u) \int_{-\infty}^t dW_s R(t+u-s) \quad (26)$$

with $f(0) = 1$ such that $z_t = z_{t,0}$. Differentiating Eq. (26) we then obtain the partial differential equation

$$dz_{t,u} = \left[\frac{\partial z_{t,u}}{\partial u} - \frac{f'(u)}{f(u)} z_{t,u} \right] dt + f(u) R(u) dW_t \quad (27)$$

which can be solved in concert with Eqs. (19) and (21).

Obviously implementation of the rather sophisticated approach outlined in this section is quite a bit more involved than that for exponential type memory functions. However, all aspects of this treatment are exact and similar calculations have been shown effective for other types of integrodifferential equations[24]. Hence, we will leave a detailed study of this approach to a subsequent manuscript.

III. NONLINEAR NMQSD EQUATIONS

While we have obtained mostly good convergence and accuracy using the linear NMQSD equation, the theory can also be formulated in terms of a norm preserving nonlinear VDE. The introduction of norm-preserving equations is important since their solutions may have physical significance[32]. More practically, the norm-preserving equations in many instances yield faster convergence of the mean with the number of trajectories. The norms of the non-norm-preserving equations go to zero with probability one and so for long time dynamics, contributions to the mean tend to come from a few unusual trajectories potentially making convergence slow. The computational cost per trajectory for the norm-preserving equations is only a little greater than that of Eqs. (12). Moreover, the non-norm-preserving equations are themselves nonlinear and so there is no apparent drawback to the norm-preserving reformulation of NMQSD.

The norm-preserving formulation of NMQSD is obtained via a two step process consisting of a Girsanov transformation followed by normalization of the wave vector. The details are given in Ref. [18]. Defining U_t through $\psi_t = U_t\psi_0$, and substituting into the norm-preserving wave equation of Ref. [18], it can be deduced that

$$\begin{aligned} \frac{dU_t}{dt} &= -iHU_t + (z_t + \int_0^t ds \alpha^*(t,s)\langle L^\dagger \rangle_s) (L - \langle L \rangle_t) U_t \\ &\quad - (L^\dagger - \langle L^\dagger \rangle_t) U_t \int_0^t ds \alpha(t,s)U_s^{-1}LU_s \\ &\quad + \langle \psi_0 | U_t^\dagger (L^\dagger - \langle L^\dagger \rangle_t) U_t \int_0^t ds \alpha(t,s)U_s^{-1}LU_s | \psi_0 \rangle U_t \end{aligned} \quad (28)$$

where $\langle L \rangle_t = \langle \psi_t | L | \psi_t \rangle$. Note that U_t now depends on the initial wave function ψ_0 . As in the linear case there is also an equation for the inverse U_t^{-1} ,

$$\frac{dU_t^{-1}}{dt} = iU_t^{-1}H - (z_t + \int_0^t ds \alpha^*(t,s)\langle L^\dagger \rangle_s) U_t^{-1} (L - \langle L \rangle_t)$$

$$\begin{aligned}
& + U_t^{-1}(L^\dagger - \langle L^\dagger \rangle_t) U_t \int_0^t ds \alpha(t, s) U_s^{-1} L U_s U_t^{-1} \\
& - \langle \psi_0 | U_t^\dagger (L^\dagger - \langle L^\dagger \rangle_t) U_t \int_0^t ds \alpha(t, s) U_s^{-1} L U_s | \psi_0 \rangle U_t^{-1}. \tag{29}
\end{aligned}$$

These integrodifferential equations can again be re-expressed as sets of ordinary or partial differential equations. Again we consider two cases.

A. Sum of exponentials

If the memory function can be expressed as a sum of exponentials via (13) then we can again define operators

$$V_{t,j} = \int_0^t ds A_j e^{-\gamma_j(t-s)} e^{-i\omega_j(t-s)} U_s^{-1} L U_s \tag{30}$$

such that the full set of equations in ordinary differential form becomes

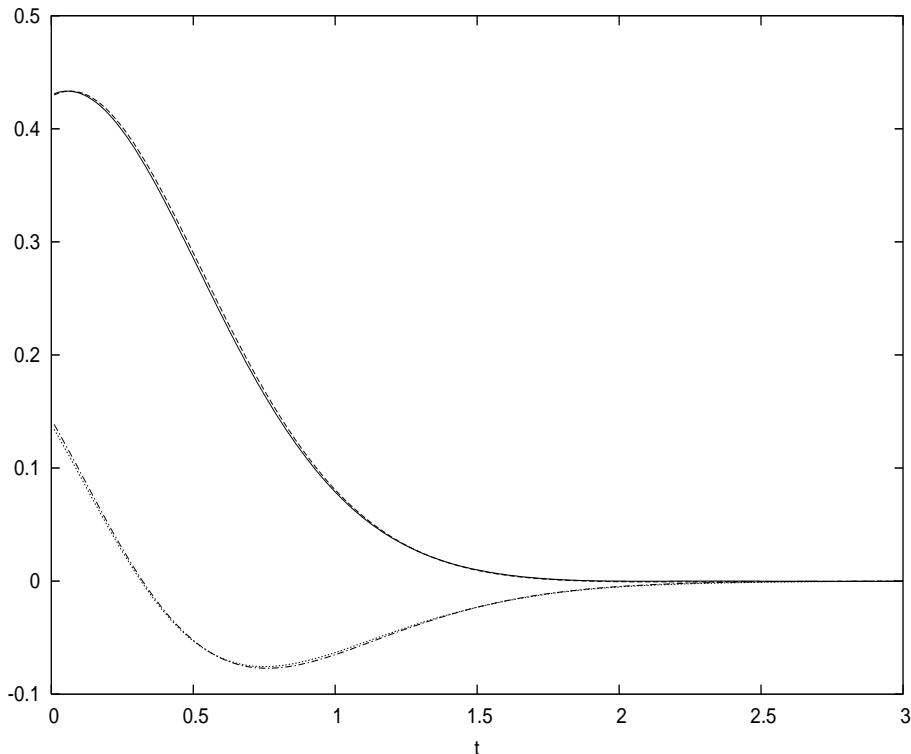
$$\begin{aligned}
\frac{dU_t}{dt} &= -iH U_t + (z_t + \sum_{j=1}^m y_{t,j}) (L - \langle L \rangle_t) U_t \\
& - (L^\dagger - \langle L^\dagger \rangle_t) U_t \sum_{j=1}^m V_{t,j} \\
& + \langle \psi_0 | U_t^\dagger (L^\dagger - \langle L^\dagger \rangle_t) U_t \sum_{j=1}^m V_{t,j} | \psi_0 \rangle U_t \\
\frac{dU_t^{-1}}{dt} &= iU_t^{-1} H - (z_t + \sum_{j=1}^m y_{t,j}) U_t^{-1} (L - \langle L \rangle_t) \\
& + U_t^{-1} (L^\dagger - \langle L^\dagger \rangle_t) U_t \sum_{j=1}^m V_{t,j} U_t^{-1} \\
& - \langle \psi_0 | U_t^\dagger (L^\dagger - \langle L^\dagger \rangle_t) U_t \sum_{j=1}^m V_{t,j} | \psi_0 \rangle U_t^{-1} \\
\frac{dV_{t,j}}{dt} &= -(\gamma_j + i\omega_j) V_{t,j} + A_j U_t^{-1} L U_t \\
\frac{dy_{t,j}}{dt} &= -(\gamma_j - i\omega_j) y_{t,j} + A_j \langle L^\dagger \rangle_t \tag{31}
\end{aligned}$$

where $y_{t,j} = \int_0^t ds A_j e^{-\gamma_j(t-s)} e^{i\omega_j(t-s)} \langle L^\dagger \rangle_s$. A key to efficient numerical implementation of these equations is evaluation and temporary storage of $\sum_{j=1}^m V_{t,j}$ from which $U_t \sum_{j=1}^m V_{t,j}$, and $(L^\dagger - \langle L^\dagger \rangle_t) U_t \sum_{j=1}^m V_{t,j}$, $\langle \psi_0 | U_t^\dagger (L^\dagger - \langle L^\dagger \rangle_t) U_t \sum_{j=1}^m V_{t,j} | \psi_0 \rangle$ can be evaluated. Again $dU_t^{-1}/dt = -U_t^{-1} dU_t/dt U_t^{-1}$ should be used to find dU_t^{-1}/dt . The conservation law $\langle \psi_t | \psi_t \rangle = 1$ proves very useful for debugging code for Eqs. (31). When $\text{Tr}\{L\} = 0$ an additional check can be made to verify that $\text{Tr}\{V_{t,j}\} = 0$.

1. *Example IIIA*

Consider again the case where $H = (\omega/2)\sigma_z$ and $L = \lambda\sigma_z$ and pick $\alpha(t, s) = (\gamma/2)e^{-\gamma(t-s)}$ with $\omega = 1$, $\lambda^2 = 2\omega$ and $\gamma = \omega$. For the initial condition $|\psi_0\rangle = \frac{1+2i}{\sqrt{7}}|1\rangle + \frac{1+i}{\sqrt{7}}|2\rangle$ we calculated $\langle 1|\rho_t|2\rangle$ using Eqs. (17) and an average over 10000 trajectories. In Fig. 8 we plot the real (solid curve) and imaginary (dotted curve) parts vs time against the corresponding known exact results[18] (dashed and dot-dashed, respectively). Once again we used the

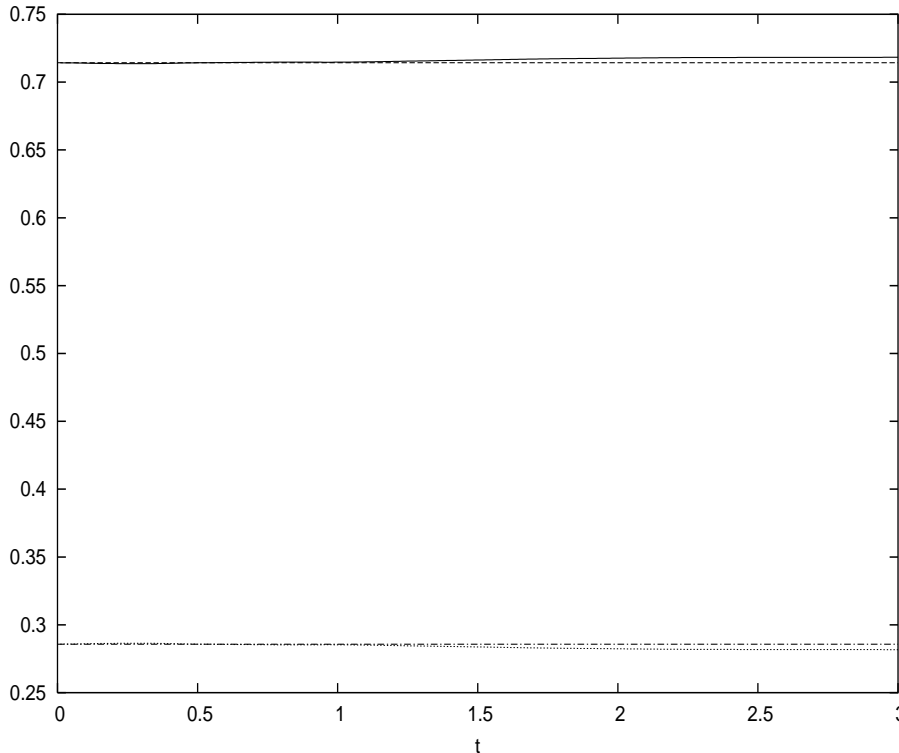
FIG. 8: $\langle 1|\rho_t|2\rangle$ for Example IIIA



ANISE software[26] to solve the equations. Norm was preserved to machine precision for individual trajectories.

As in the case of the non-norm-preserving equations, convergence of the off-diagonal matrix element is good with 10000 trajectories. In Fig. 9 we show the diagonal matrix elements $\langle 1|\rho_t|1\rangle$ and $\langle 2|\rho_t|2\rangle$. For the non-norm-preserving equations we obtained poor convergence for 10000 trajectories. However, for the norm-preserving equations the convergence is quite good. The non-preserving equations do indeed seem to lead to faster convergence as claimed in Ref. [18].

FIG. 9: $\langle 1|\rho_t|1\rangle$ and $\langle 2|\rho_t|2\rangle$ for Example IIIA



2. Example IIIB

Now consider $H = (\omega/2)\sigma_z$ and $L = (\lambda/2)(\sigma_x - i\sigma_y)$ and again pick $\alpha(t, s) = (\gamma/2)e^{-\gamma(t-s)}$ with $\omega = 1$, $\lambda^2 = 2\omega$ and $\gamma = \omega$. For the initial condition $|\psi_0\rangle = \frac{1}{\sqrt{2}}(|1\rangle + |2\rangle)$ we calculated $\langle 1|\rho_t|2\rangle$ using Eqs. (17) and an average over 10000 trajectories. The real and imaginary parts (solid and dotted) are plotted in Fig. 10 against exact results (dashed and dot-dashed). Agreement is good. In Fig. 11 we show the numerically computed diagonal matrix elements $\langle 1|\rho_t|1\rangle$ and $\langle 2|\rho_t|2\rangle$ (solid and dotted) against exact results (dashed and dot-dashed). Convergence is again good.

3. Example IIIC

Now consider a harmonic oscillator subsystem with $H = \omega a^\dagger a$ and $L = \lambda a$. We chose an initial condition $|\psi_0\rangle = \frac{1+2i}{\sqrt{7}}|1\rangle + \frac{1+i}{\sqrt{7}}|2\rangle$ and picked $\alpha(t, s) = (\gamma/2)e^{-\gamma(t-s)}$ with $\omega = 1$, $\lambda = \omega$ and $\gamma = \omega$. Convergence is rapid and so we used only 1000 trajectories. The cpu time was about 12 minutes on a 600 MHz Alpha processor. In Fig. 12 we plot the real and imaginary

FIG. 10: $\langle 1|\rho_t|2\rangle$ for Example IIIB

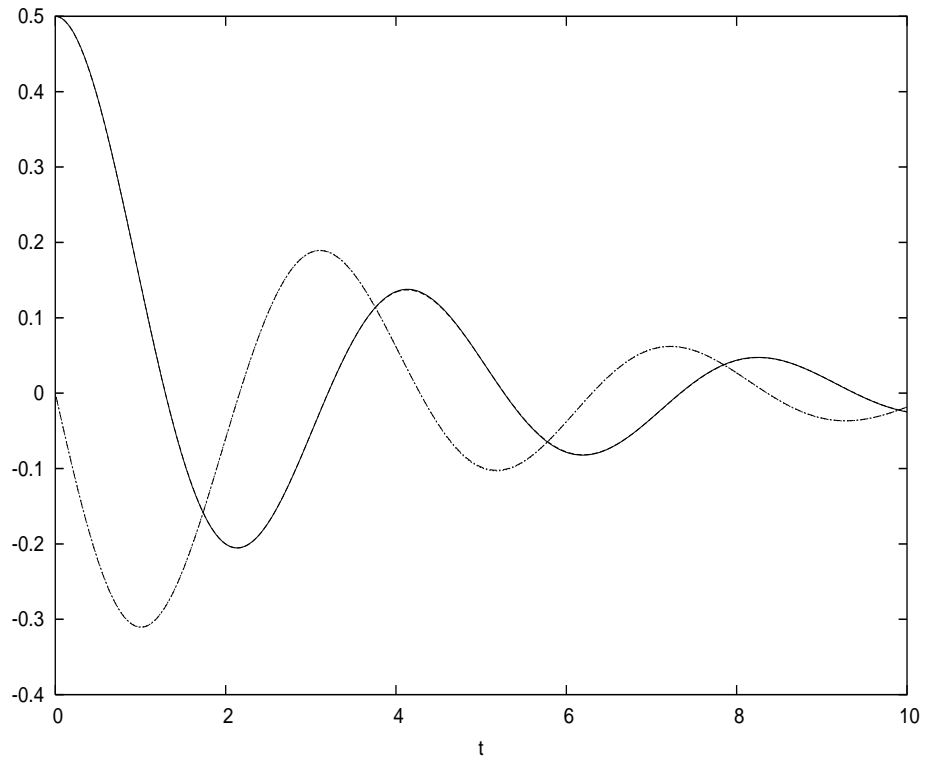
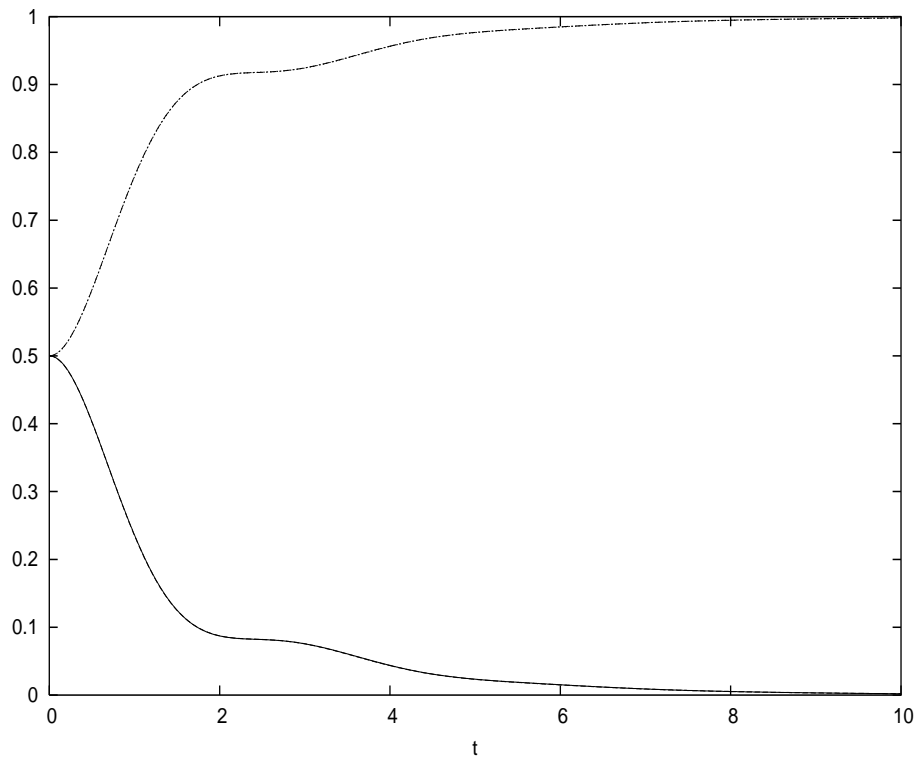
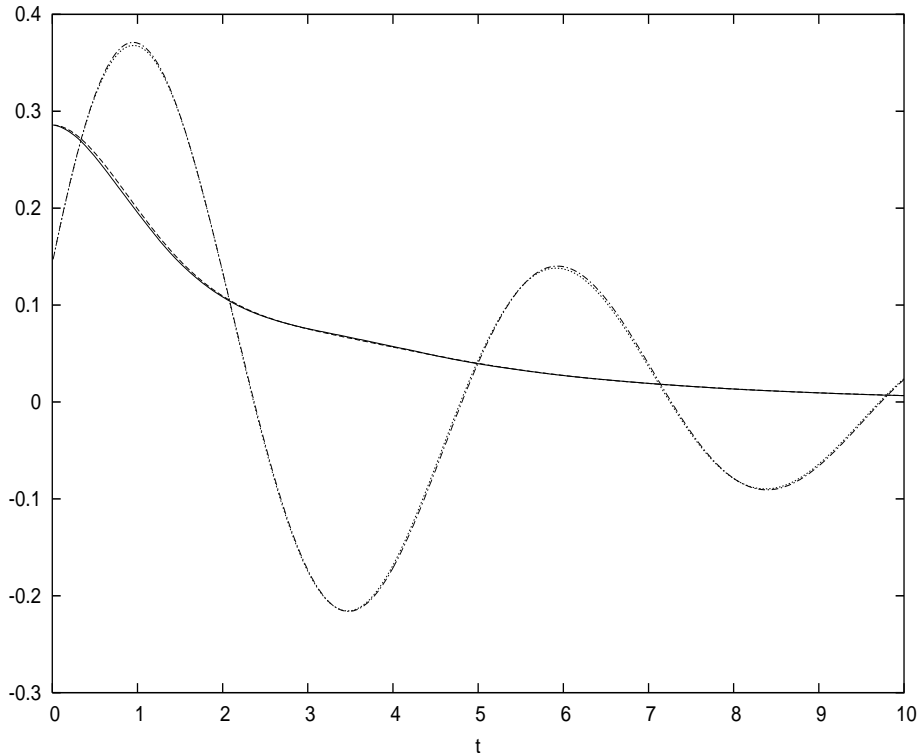


FIG. 11: $\langle 1|\rho_t|1\rangle$ and $\langle 2|\rho_t|2\rangle$ for Example IIIB



parts (solid and dotted) of $\langle 1|\rho_t|2\rangle$ vs their corresponding exact real and imaginary parts (dashed and dot-dashed). In Fig. 13 we show the diagonal matrix elements $\langle 1|\rho_t|1\rangle$ and $\langle 2|\rho_t|2\rangle$ (solid and dotted) plotted against their corresponding exact results (dashed and dot-dashed). The results are good.

FIG. 12: $\langle 1|\rho_t|2\rangle$ for Example IIIC



B. General memory function

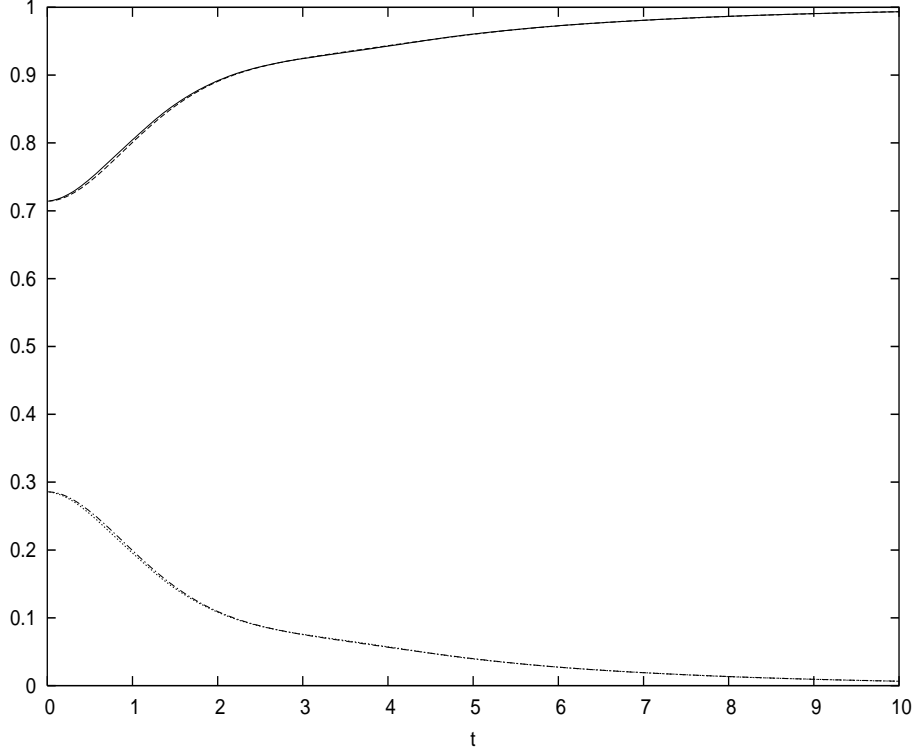
When the memory function cannot be represented as a sum of exponentials of the previous form, it is again possible to rewrite the equations in partial differential form. We again introduce a new variable u and define

$$V_{t,u} = \int_0^t ds \alpha(t+u, s) U_s^{-1} L U_s \quad (32)$$

such that the new set of equations has partial differential form

$$\begin{aligned} \frac{dU_t}{dt} &= -i H U_t + (z_t + y_{t,0}) (L - \langle L \rangle_t) U_t \\ &\quad - (L^\dagger - \langle L^\dagger \rangle_t) U_t V_{t,0} \end{aligned}$$

FIG. 13: $\langle 1|\rho_t|1\rangle$ and $\langle 2|\rho_t|2\rangle$ for Example IIIC



$$\begin{aligned}
& + \langle \psi_0 | U_t^\dagger (L^\dagger - \langle L^\dagger \rangle_t) U_t V_{t,0} | \psi_0 \rangle U_t \\
\frac{dU_t^{-1}}{dt} &= iU_t^{-1}H - (z_t + y_{t,0}) U_t^{-1} (L - \langle L \rangle_t) \\
& + U_t^{-1} (L^\dagger - \langle L^\dagger \rangle_t) U_t V_{t,0} U_t^{-1} \\
& - \langle \psi_0 | U_t^\dagger (L^\dagger - \langle L^\dagger \rangle_t) U_t V_{t,0} | \psi_0 \rangle U_t^{-1} \\
\frac{dV_{t,u}}{dt} &= \alpha(t+u, t) U_t^{-1} L U_t + \frac{\partial V_{t,u}}{\partial u} \\
\frac{dy_{t,u}}{dt} &= \alpha^*(t+u, t) \langle L^\dagger \rangle_t + \frac{\partial y_{t,u}}{\partial u}
\end{aligned} \tag{33}$$

where

$$y_{t,u} = \int_0^t ds \alpha^*(t+u, s) \langle L^\dagger \rangle_s. \tag{34}$$

The same considerations regarding adding a damping factor and generation of the noise z_t , discussed in section IIB, apply here without modification.

IV. NEW EXAMPLES

We now consider three new problems which it was previously impossible to explore exactly using NMQSD. Our treatment of these examples is not meant to be exhaustive. We simply

wish to show that interesting issues can be explored using the computational implementation of NMQSD introduced in sections II and III. We choose to use the norm-preserving version of the theory. This improves convergence and also allows us to study individual trajectories, which may have some physical significance[32]. Specifically, it has been shown that NMQSD can be interpreted as a hidden variable theory in which the noise z_t represents a hidden-variable of the bath[32]. We shall see that individual trajectories do indeed behave in ways consistent with physical intuition. Whether their non-quantum-mechanical statistical properties (e.g. $M[|\langle\psi_0|\psi_t\rangle|^2] = \langle\psi_0|\rho_t|\psi_0\rangle$ can be predicted with standard quantum theory, while $M[|\langle\psi_0|\psi_t\rangle|^4] - M[|\langle\psi_0|\psi_t\rangle|^2]^2$ cannot) are in agreement with experiment remains an open and interesting question.

A. Example IVA

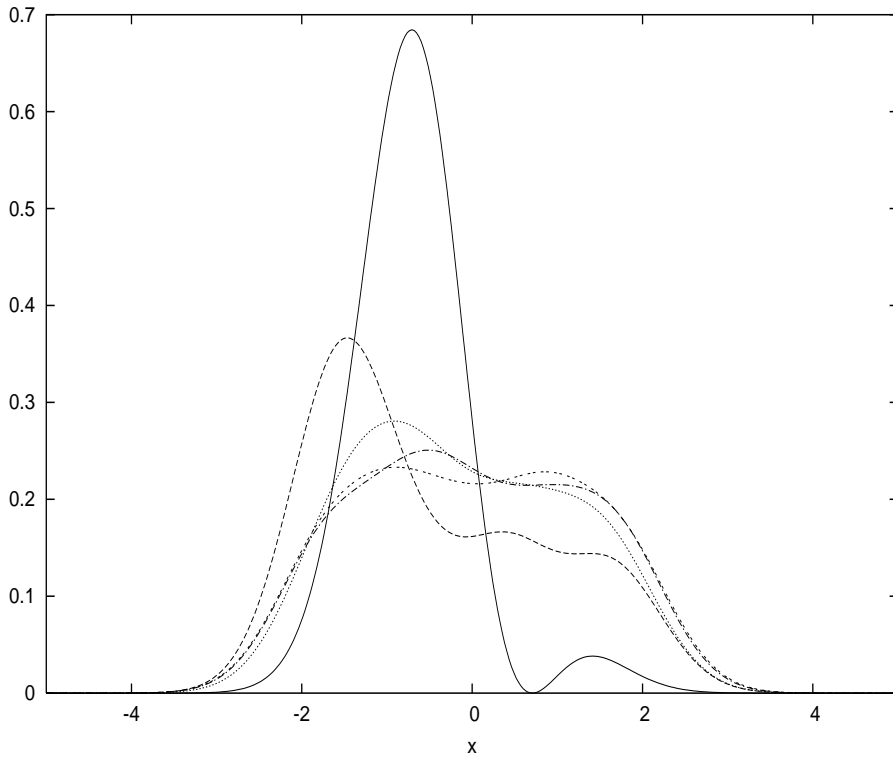
Here we consider the dynamics of a symmetric double well representing a reaction coordinate of an isomeric or chiral molecule, interacting with the radiation field. Of course realistic chemical environments contain sources of decoherence other than the radiation field, but the example is still of interest. When an ensemble of such systems is prepared in an initial achiral state, interaction with the radiation field is expected to drive the population to a symmetric final distribution. Indeed, clocks for dating amino acids have been proposed on this basis[33]. When the barrier height is low (e.g. in NHDT) individual molecules are observed in states which are superpositions of left and right handed states (e.g. the ground state of the double well). When the barrier height is large, individual molecules are found in left handed states or right handed states but not normally in superpositions (although superpositions can in principle be prepared[34]). This is unusual because the eigenstates of the double well are superpositions of left and right handed states. Environment induced superselection rules are sometimes invoked to explain this effect[35, 36]. We will now explore the predictions of NMQSD in these two cases.

Consider a quartic oscillator subsystem with $H = \omega[a^\dagger a - (3/8)(a^\dagger + a)^2 + \epsilon(a^\dagger + a)^4]$ and $L = \lambda a$. This Hamiltonian corresponds to a symmetric double well potential and so could represent a reaction coordinate for isomerization or racemization of a molecule. We choose an initial condition $|\psi_0\rangle = \frac{1}{\sqrt{2}}(|0\rangle - |1\rangle)$ which means the particle is initially localized in the left well, and pick $\alpha(t, s) = (\gamma/2)e^{-\gamma(t-s)}$ with $\omega = 1$, $\epsilon = \hbar\omega/E_b$, $\lambda = \omega$ and $\gamma = \omega$ where E_b

is the activation energy of the barrier. The parameter ϵ controls the effective barrier height.

First consider the case where $\epsilon = .692$, which is typical for proton transfer isomerization[37]. In Fig. 14 we plot the probability density $\langle x|\rho_t|x\rangle$ against x (in units of $\sqrt{\hbar/m\omega}$) for times $t = 0$ (solid), 2 (dashed), 4 (dotted), 6 (dot-dashed) and 12 (double-dashed). Dissipation and decoherence drive the population from a nearly pure left-handed state to a symmetric mixture. The calculation was performed in a basis set of the lowest five harmonic oscillator states. A total of 1000 trajectories were included in the average. The calculation again took about ten minutes. In Fig. 15 we plot $\langle x|\rho_t|x\rangle$ against x , com-

FIG. 14: Relaxation of $\langle x|\rho_t|x\rangle$ vs x for Example IVA with $\epsilon = .692$



puted for 1000 and 10000 trajectories, at times $t = 2$ (solid and dashed), 4 (dotted and dot-dashed) and 12 (double-dashed and triple-dashed). Convergence is again quite good for 1000 trajectories.

Assuming that individual trajectories may have some physical significance, as has been suggested[32], it is worth examining a few to see whether their dynamics makes intuitive sense. For this moderate barrier case we anticipate asymptotic states which are mixtures of left and right. In fact as we see in Fig. 16, where we plot densities for individual trajectories at time $t = 12$, some trajectories do lead to superpositions. However, some also remain

FIG. 15: Convergence of $\langle x|\rho_t|x\rangle$ vs x for Example IVA with $\epsilon = .692$

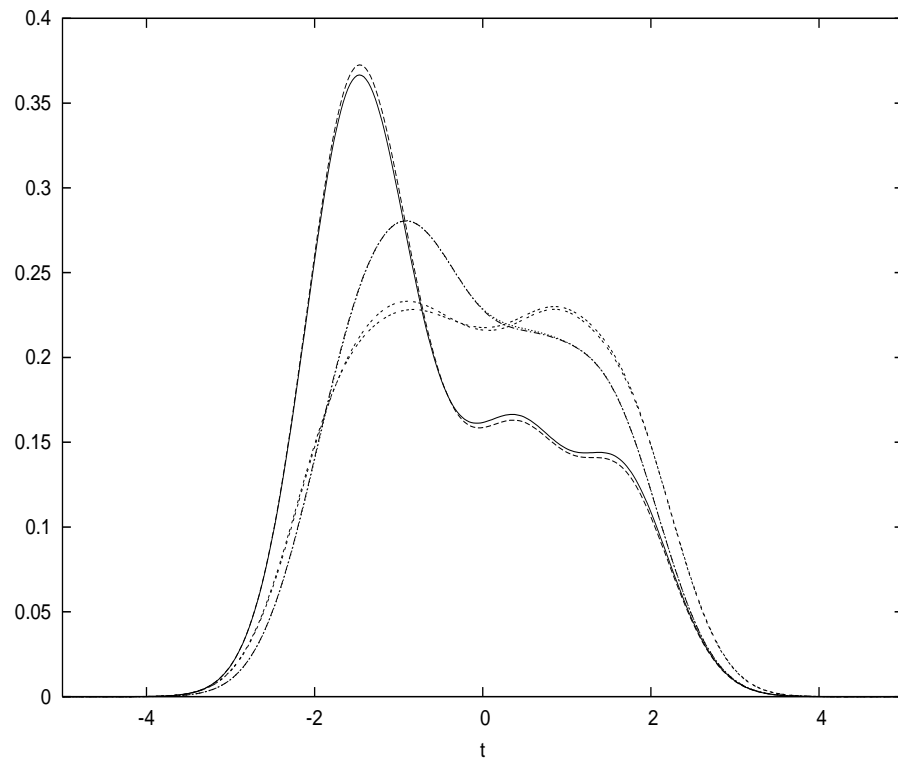
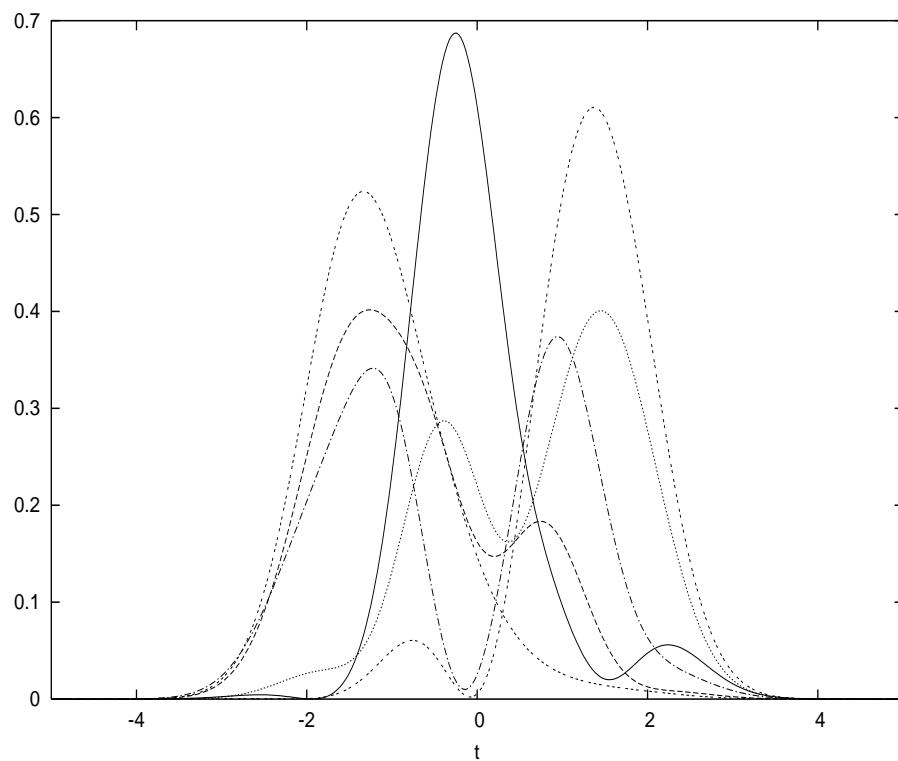


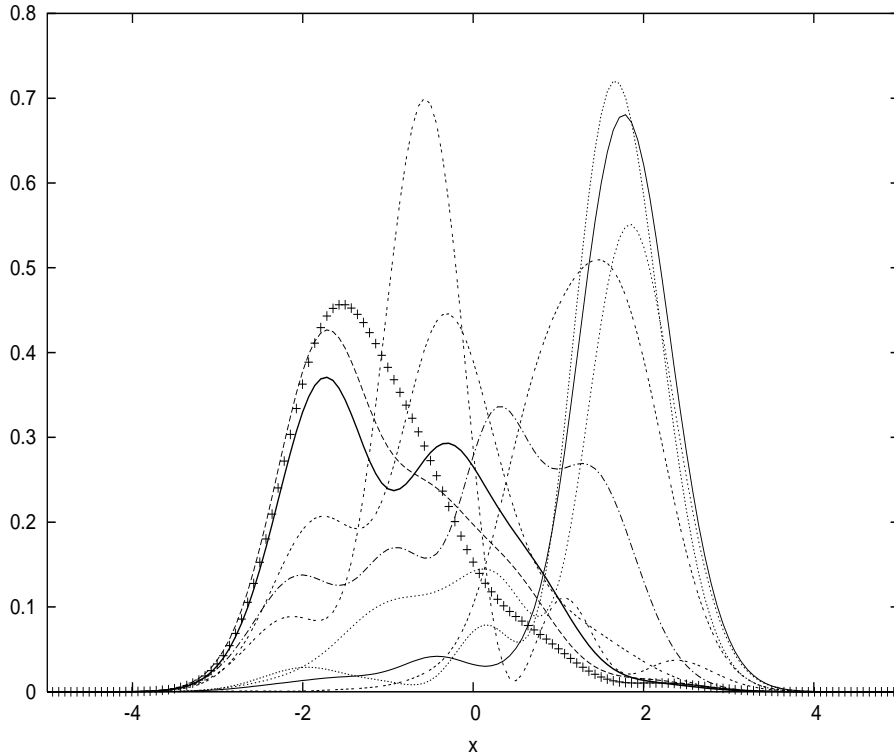
FIG. 16: $\langle x|\psi_t\rangle\langle\psi_t|x\rangle$ vs x for individual trajectories at $t = 12$, for Example IVA with $\epsilon = .692$



strongly localized on the left of the barrier, while others have made a jump to the right. Thus, superselection appears to begin to play a role even for moderate barriers.

Now consider the case of a higher barrier, where $\epsilon = .1$, which is still very modest compared to that expected for large chiral molecules. In Fig. 17 we again plot $\langle x|\psi_t\rangle\langle\psi_t|x\rangle$ vs x for individual trajectories, this time at $t = 14$. For this higher barrier the individual

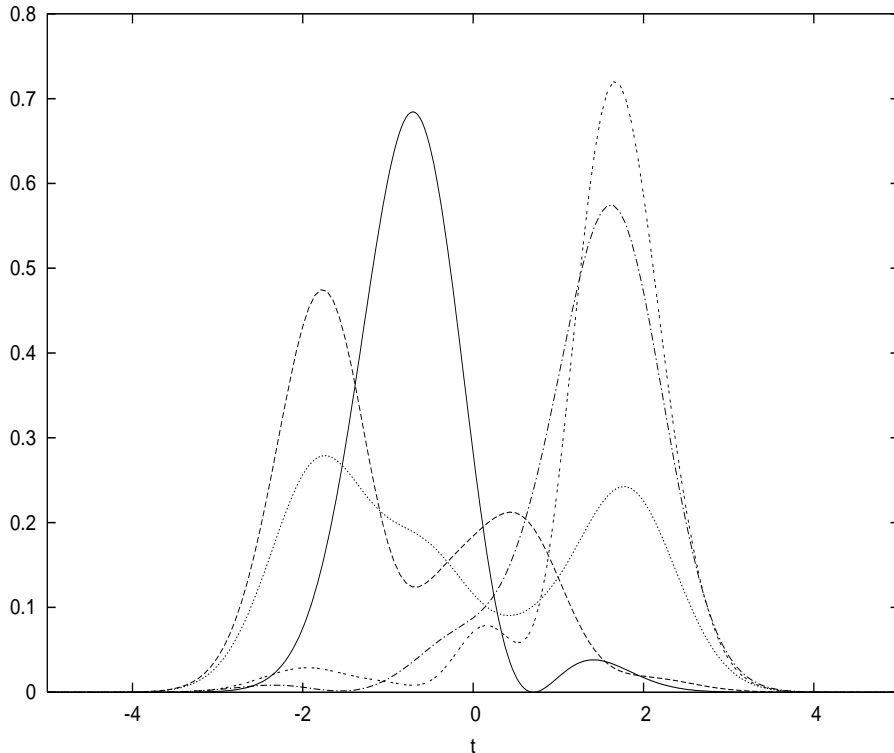
FIG. 17: $\langle x|\psi_t\rangle\langle\psi_t|x\rangle$ vs x for individual trajectories at $t = 14$, for Example IVA with $\epsilon = .1$



densities are more strongly chiral, with most strongly localized on one side of the barrier or the other. The only state even close to an equal superposition of left and right is the dot-dashed curve. These results support the notion of the emergence of a superselection rule favoring states localized on one side of the barrier or the other over superpositions.

In Fig. 18 we follow a single trajectory as it tunnels from one side of the barrier to the other. The densities indicated are for times $t = 0$ (solid), 2 (dashed), 4 (dotted), 6 (dot-dashed) and 14 (double-dashed). The tunneling process appears to start almost immediately and is effectively over by $t = 6$. In other cases tunneling had already occurred by $t = 2$. This apparent discrepancy invites further scrutiny in light of the many studies predicting well defined tunneling times[38].

FIG. 18: $\langle x|\psi_t\rangle\langle\psi_t|x\rangle$ vs x for an individual trajectory at various times, for Example IVA with $\epsilon = .1$



B. Example IVB

Here we consider a two-level atom immersed in the radiation field of a dielectric band gap. This model has recently been studied using approximations to the NMQSD equations[21]. In an interaction picture, rotating with the subsystem Hamiltonian, $H = 0$ and $L = \frac{i\lambda}{2}(\sigma_x - i\sigma_y)$. The memory function is given by

$$\alpha(t, s) = e^{i(\omega-A)(t-s)} [J_0(\frac{B}{3}(t-s))]^3 \quad (35)$$

where $\hbar\omega$ is the excitation energy of the atom, a band of allowed frequencies lies between $A - B$ and $A + B$, the gap lies between 0 and $A - B$, and J_0 is the Bessel function of the first kind of order 0. We scale time in units of \hbar/λ and energy in units of λ . In these units we set $\omega = 10$, $B = 5$ and we will consider two values of A corresponding to ω in the band ($A = \omega$) and in the gap ($A = \omega + B + 1$).

A_j	γ_j	$\pm\omega_j^0$
6.636×10^{-2}	3.3602×10^{-3}	0.9598
1.597×10^{-2}	0.2301	4.4870
6.513×10^{-2}	1.0000×10^{-5}	0.5762
2.112×10^{-2}	0.2003	4.0230
6.551×10^{-2}	1.0000×10^{-5}	0.1924
2.202×10^{-2}	0.1335	3.6070
3.460×10^{-2}	2.1033×10^{-2}	2.4534
4.018×10^{-2}	2.1043×10^{-4}	2.0778
2.619×10^{-2}	8.8754×10^{-2}	3.2106
5.637×10^{-2}	1.0000×10^{-5}	1.7026
2.731×10^{-2}	3.8032×10^{-2}	2.8303
6.388×10^{-2}	1.0000×10^{-5}	1.3391

We fitted (35) to the form (13) using nonlinear least squares, where ω_j come in pairs $\omega_j = \omega - A + \omega_j^0$ and $\omega_j = \omega - A - \omega_j^0$ for each A_j and γ_j . The resulting parameters are given in Table 1. In Fig. 19 we plot (35) (solid curve) against (13) (dashed), which shows that the fit is quite satisfactory.

We chose an initial state $|\psi_0\rangle = |1\rangle$ which corresponds to an excited 2-level atom (note that our convention for labeling the states is the reverse of that in Ref. [21]). We calculated $\langle 1|\rho_t|1\rangle$ and $\langle 2|\rho_t|2\rangle$ using 1000 trajectories for ω in the band ($\omega = A$, solid and dotted curves) and ω in the gap ($\omega = A + B + 1$, dashed and dot-dashed curves). These quantities are plotted in Fig. 20. When ω is in the band, emission of a photon occurs, and the two-level atom relaxes to its ground state. When ω is in the gap the system evolves toward a statistical superposition of the two states (i.e. $\langle 1|\rho_t|2\rangle = 0$) which is weighted toward the excited state. It should however be remembered that each individual trajectory represents a pure state and so has a density matrix with nonzero off-diagonal elements. In Fig. 21 we show the density matrix elements $\langle 1|\rho_t|1\rangle$ (solid) and $\langle 2|\rho_t|2\rangle$ (dashed) and the real and imaginary parts of $\langle 1|\rho_t|2\rangle$ (dotted and dot-dashed) for an individual trajectory with ω in the gap. Individual trajectories thus evolve toward a *coherent* superposition of the excited and ground states, with the excited state weighted more heavily.

FIG. 19: $\alpha(t, 0)$ for Example IVB with $\omega = A$

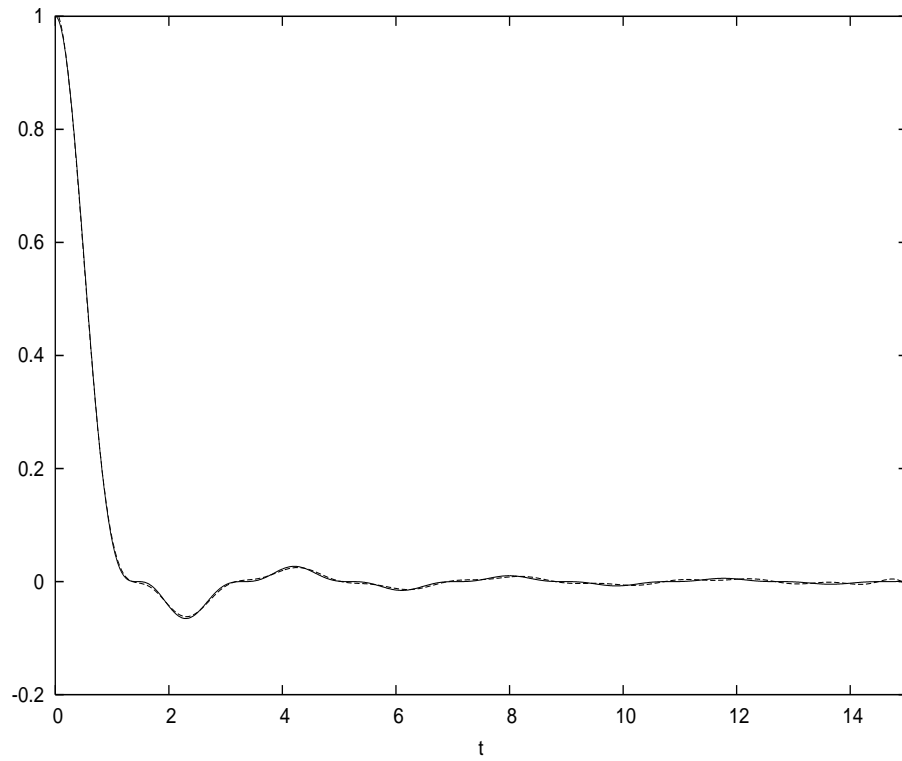


FIG. 20: $\langle 1|\rho_t|1\rangle$ and $\langle 2|\rho_t|2\rangle$ for Example IVB with $\omega = A$ (solid and dotted) and $\omega = A + 1$ (dashed and dot-dashed)

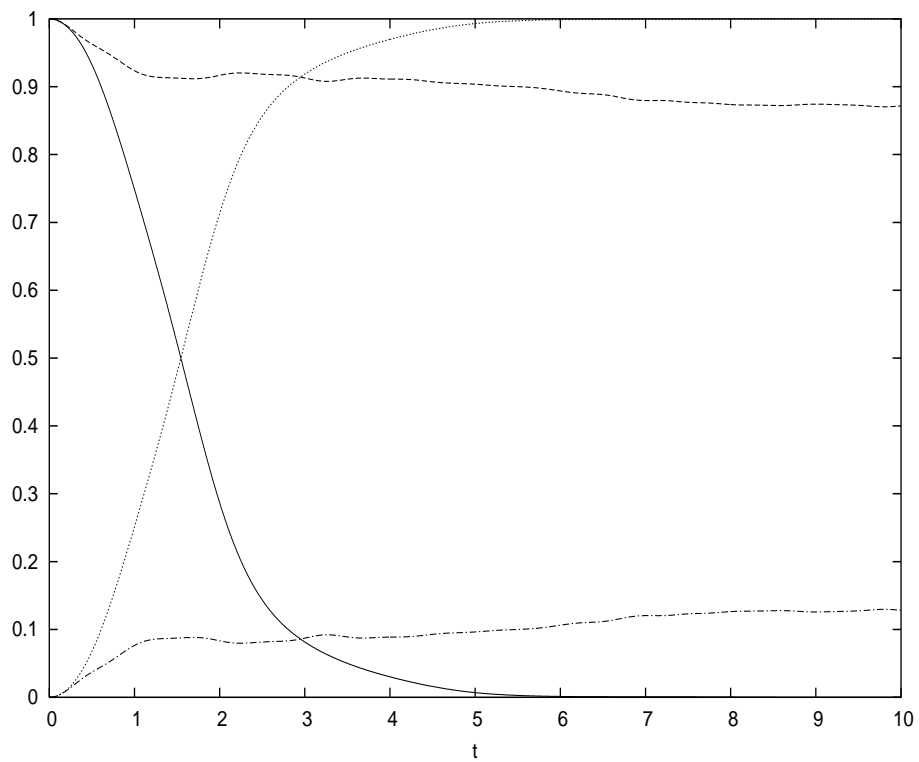
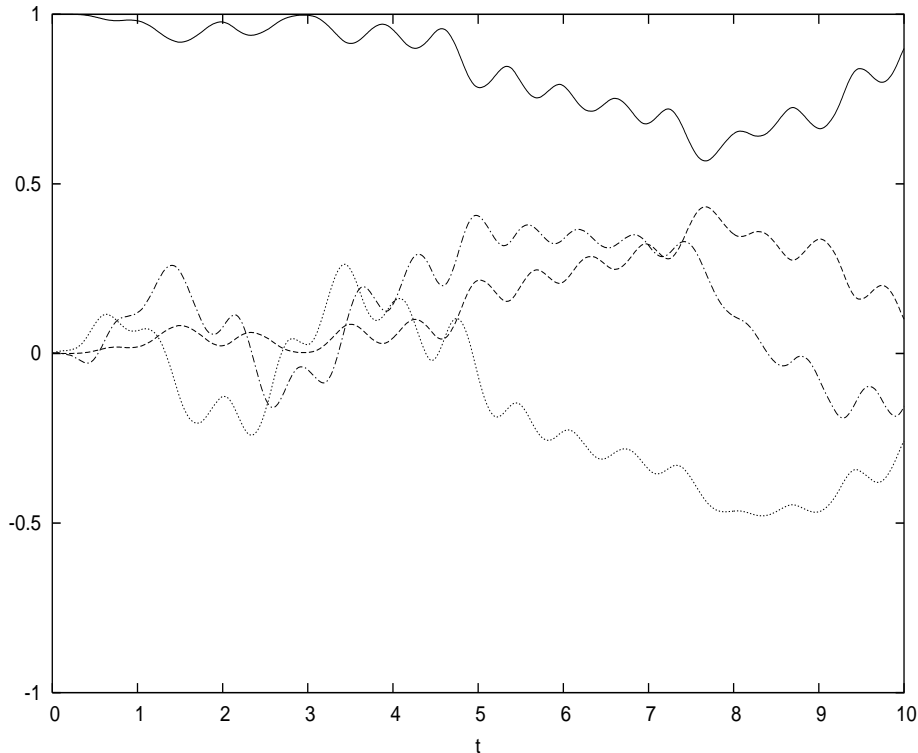


FIG. 21: $\langle 1|\rho_t|1\rangle$, $\langle 2|\rho_t|2\rangle$ and $\langle 1|\rho_t|2\rangle$ for a single trajectory of Example IVB



C. Example IVC

Finally, we consider a three-level system ($|1\rangle$ with energy $E_1 = 0$ in eV, $|2\rangle$ with $E_2 = 4.4$, and $|3\rangle$ with $E_3 = 0$) representing three electronic states of a Mg^+ ion in an ion trap, which is driven by a laser resonant with the transition between levels 1 and 2. This system has been quite extensively studied[1, 2, 3, 4, 5] due to the interesting phenomenon of intermittent fluorescence exhibited by the ion. The ion which normally cycles between states 1 and 2 occasionally jumps into the dark state 3 giving rise to periods where no fluorescence is observed. These stochastic jumps have been observed experimentally[1] and theoretically[2, 5] over a time scale with millisecond resolution. It has been suggested that such stochastic jumps might occur on all time scales[5]. Here we show that NMQSD predicts jump phenomena on a picosecond timescale consistent with this scenario.

The effective Hamiltonian in a frame rotating with the Hamiltonian of the isolated ion has the form

$$H = (\Omega/2)(|1\rangle\langle 2| + |2\rangle\langle 1|) \quad (36)$$

where Ω is the Rabi frequency of the 1-2 transition. The coupling operators L_i for $i = 1, \dots, 4$

have the forms

$$\begin{aligned}
L_1 &= \lambda_{12}|1\rangle\langle 2| \\
L_2 &= \lambda_{13}|1\rangle\langle 3| \\
L_3 &= \lambda_{31}|3\rangle\langle 1| \\
L_4 &= \lambda(|1\rangle\langle 1| - |3\rangle\langle 3|).
\end{aligned}
\tag{37}$$

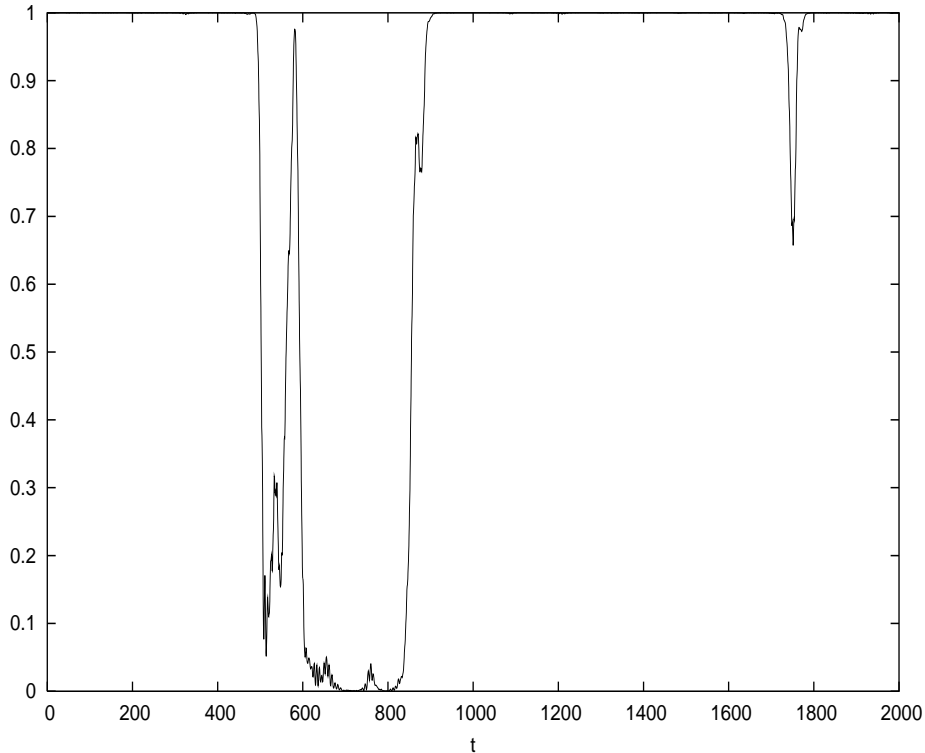
The parameters were chosen as $\lambda_{12} = \sqrt{\gamma/\tau}$, $\lambda_{13} = \sqrt{R_-/\tau}$, $\lambda_{31} = \sqrt{R_+/\tau}$ where γ is the spontaneous decay rate for the 2-1 transition and R_- and R_+ are the rates out of and into the dark state 3, respectively[3]. It has been shown that $R_- = 8\Omega^2\gamma/9\alpha^2$ and $R_+ = \Omega^2\gamma/18\alpha^2$ where α denotes a Zeeman splitting[3]. Finally, the λ operator arises due to interaction with the photodetectors. To reproduce the results of Ref. [3] in the Markovian limit we set $\tau = \int_0^\infty \text{Re } \alpha(t)dt$. The memory function, which is common to the four noises, was calculated with a Debye distribution of frequencies and for a temperature of about .1 K. We chose time units $10^{-3}\gamma^{-1}$ - roughly a picosecond since $\gamma = 2\pi 43$ MHz[3] - in terms of which we set $\alpha = 12.1$, $\Omega = 2$, $\lambda_{12} = 10^{-3}/\sqrt{\tau}$, $\lambda_{31} = \sqrt{1/18}\Omega/(\alpha\sqrt{\tau})$, $\lambda_{13} = \sqrt{8/9}\Omega/(\alpha\sqrt{\tau})$ and $\lambda = .22/sqrt{\tau}$. We calculated that $\tau = 509$ from the 5 term non-linear least squares fit to the memory function, although the principle decay occurs over the first 50 time units. The dynamics is thus quite strongly non-Markovian.

In Fig. 22 we show the occupation probability of the 1-2 manifold $|\langle 1|\psi_t\rangle|^2 + |\langle 2|\psi_t\rangle|^2$ plotted against time. At various times and for various lengths of time this probability approaches zero indicating that the ion has jumped to the dark state 3. A more detailed analysis of the statistical properties of the dark periods will be presented elsewhere.

V. DISCUSSION

Non-Markovian quantum state diffusion (NMQSD), being an exact unraveling of the master equation for an arbitrary subsystem interacting linearly with a boson bath, potentially has a wide range of applications in quantum optics. This potential has not been realized to any significant extent due to the difficulty of solving - even numerically - the variational-differential evolution equation. In fact the development of NMQSD has not led to the exact solution of any new problems. In this manuscript we have shown how the variational-differential equations (VDEs) of NMQSD can be exactly rewritten as integrodifferential

FIG. 22: $|\langle 1|\psi_t\rangle|^2 + |\langle 2|\psi_t\rangle|^2$ vs t for a single trajectory of Example IVC



equations which can in turn be rewritten as ordinary or partial differential equations. We illustrated application of the new NMQSD equations by solving a number of problems for which exact solutions were already known. Both linear and nonlinear versions of NMQSD were studied. We found that both versions worked well and yielded high accuracy solutions. Finally, we applied the method to three previously unsolvable problems (tunneling in a double well, two-level atom in a photonic band gap, and intermittent fluorescence in a driven three-level ion) to show that interesting work can be done with the reformulated theory. We anticipate that other interesting applications of NMQSD will emerge now that the equations can be solved in a systematic fashion.

The authors acknowledge the support of the Natural Sciences and Engineering Research Council of Canada.

-
- [1] H.F. Powell, M.A. van Eijkelenborg, W. Irvine, D.M. Segal and R.C. Thompson, *J. Phys. B* 35, 205 (2002); R.G. Hulet, D.J. Wineland, J.C. Bergquist and W.M. Itano, *Phys. Rev. A* 37, 4544 (1988).

- [2] D.T. Pegg and P.L. Knight, Phys. Rev. A 37, 4303 (1988); G. Nienhuis, Phys. Rev. A 35, 4639 (1987); A. Schenzle and R.G. Brewer, Phys. Rev. A 34, 3127 (1986); R.J. Cook and H.J. Kimble, Phys. Rev. Lett. 54, 1023 (1985).
- [3] R.G. Hulet and D.J. Wineland, Phys. Rev. A 36, 2758 (1987).
- [4] M.B. Plenio and P.L. Knight, Rev. Mod. Phys. 70, 101 (1998).
- [5] N. Gisin, P.L. Knight, I.C. Percival, R.C. Thompson and D.C. Wilson, J. Mod. Opt. 40, 1663 (1993).
- [6] S. Gulde, M. Riebe, G.P.T. Lancaster, C. Becher, J. Eschner, H. Haffner, F. Schmidt-Kaler, I.L. Chuang and R. Blatt, Nature 421 (6918), 48 (2003).
- [7] C. Anastopoulos and B.L. Hu, Phys. Rev. A 62, 033821 (2000).
- [8] M. Grifoni, E. Paladino, and U. Weiss, Eur. Phys. J. B 10, 719 (1999).
- [9] B.L. Hu, J.P. Paz, and Y.H. Zhang, Phys. Rev. D 45, 2843 (1992).
- [10] F. Haake and R. Reibold, Phys. Rev. A 32, 2462 (1985).
- [11] R.P. Feynman and F.L. Vernon, Ann. Phys. (NY) 24, 118 (1963).
- [12] M. Kuno, D.P. Fromm, H.F. Hamann, A. Gallagher and D.J. Nesbitt, J. Chem. Phys. 115, 1028 (2001).
- [13] Y.-J. Jung, E. Barkai and R.J. Silbey, J. Chem. Phys. 117, 10980 (2002).
- [14] J. Wilkie, J. Chem. Phys. 115, 10335 (2001); J. Chem. Phys. 114, 7736 (2001); Phys. Rev. E 62, 8808 (2000).
- [15] C.M. Dawson, A.P. Hines, R.H. McKenzie and G.J. Milburn, Phys. Rev. A 71, 052321 (2005); X.Z. Yuan and K.D. Zhu, Euro. Phys. Lett. 69, 868 (2005); M. Lucamarini, S. Paganelli and S. Mancini, Phys. Rev. A 69, 062308 (2004); L. Tessieri and J. Wilkie, J. Phys. A 36, 12305 (2003); M. Esposito and P. Gaspard, Phys. Rev. E 68, 066113 (2003); S. Paganelli, F. dePasquale and S.M. Giampaolo, Phys. Rev. A 66, 052317 (2002); V. Wong and M. Gruebele, Chem. Phys. 284, 29 (2002).
- [16] We use the simple notation z_t rather than the physically suggestive z_t^* [32].
- [17] L. Diósi, Quantum Semiclass. Opt. 8, 309 (1996); W.T. Strunz, Phys. Lett. A 224, 25 (1996); L. Diósi and W.T. Strunz, Phys. Lett. A 235, 569 (1997).
- [18] L. Diósi, N. Gisin and W.T. Strunz, Phys. Rev. A 58, 1699 (1998)
- [19] W.T. Strunz, L. Diósi and N. Gisin, Phys. Rev. Lett. 82, 1801 (1999).
- [20] T. Yu, L. Diosi, N. Gisin, W.T. Strunz, Phys. Rev. A 60, 91 (1999).

- [21] I. de Vega, D. Alonso and P. Gaspard, *Phys. Rev. A* 71, 023812 (2005).
- [22] W.T. Strunz and T. Yu, *Phys. Rev. A* 69, 052115 (2004).
- [23] C. Meier and D.J. Tannor, *J. Chem. Phys.* 111, 3365 (1999).
- [24] J. Wilkie, *Phys. Rev. E* 68, 027701 (2003).
- [25] See for example J. Wilkie and M. Cetinbas, *Phys. Lett. A* 337, 166 (2005); J. Wilkie, *Phys. Rev. E* 70, 017701 (2004).
- [26] ANISE, commercial software for SDEs.
- [27] L. Tessieri, J. Wilkie and M. Cetinbas, *J. Phys. A* 38, 943 (2005).
- [28] V.A. Mandelshtam and H.S. Taylor, *J. Chem. Phys.* 107, 6756 (1997). Erratum, *ibid.* 109 (10), 4128 (1998).
- [29] P. Gaspard and M. Nagaoka, *J. Chem. Phys.* 13, 5676 (1999).
- [30] K.Y.R. Billah and M. Shinozuka, *Phys. Rev. A* 46, 8031 (1992); R. Mannella and V. Palleschi, *Phys. Rev. A* 46, 8028 (1992); K.Y.R. Billah and M. Shinozuka, *Phys. Rev. A* 42, 7492 (1990); R. Mannella and V. Palleschi, *Phys. Rev. A* 40, 3381 (1989); R.F. Fox, I.R. Gatland, R. Roy and G. Vemuri, *Phys. Rev. A* 38, 5938 (1988).
- [31] D.T. Colbert and W.H. Miller, *J. Chem. Phys.* 96, 1982 (1992).
- [32] J. Gambetta and H.M. Wiseman, *Phys. Rev. A* 68, 062104 (2003).
- [33] J.L. Bada, *Science* 248, 539 (1990).
- [34] J.A. Cina and R.A. Harris, *J. Chem. Phys.* 100, 2531 (1994).
- [35] M. Schlosshauer, *Rev. Mod. Phys.* 76, 1267 (2004).
- [36] A. Amann, *J. Math. Chem.* 6, 1 (1991).
- [37] N. Makri and W.H. Miller, *J. Chem. Phys.* 87, 5781 (1987).
- [38] See for example A. Nitzan, J. Jortner, J. Wilkie, A.L. Burin and M.A. Ratner, *J. Phys. Chem. B* 104, 5661 (2000); R. Landauer and T. Martin, *Rev. Mod. Phys.* 66, 217 (1994); M. Buttiker and R. Landauer, *Phys. Rev. Lett.* 49, 1739 (1982).